Sulfur-Tuned Main-Group Sb−N−C Catalysts for Selective 2-Electron and 4-Electron Oxygen Reduction

Minmin Yan, Hao Yang, Zhichao Gong, Jiarui Zhu, Christopher Allen, Tao Cheng, Huilong Fei**

M. Yan, Z. Gong, Prof. H. Fei
Advanced Catalytic Engineering Research Center of the Ministry of Education, State Key Laboratory for Chemo/Biosensing and Chemometrics, and College of Chemistry and Chemical Engineering, Hunan University, Changsha 410082, Hunan, China
E-mail: hlfei@hnu.edu.cn

Dr. H. Yang, J. Zhu, Prof. T. Cheng
Institute of Functional Nano&Soft Materials (FUNSOM), Jiangsu Key Laboratory for Carbon-Based Functional Materials & Devices, Jiangsu Key Laboratory of Advanced Negative Carbon Technologies, Soochow University, Suzhou 215123, Jiangsu, China
Email: tcheng@suda.edu.cn

Dr. C. Allen
Department of Materials, University of Oxford, Parks Road, Oxford OX1 3PH, UK, and Electron Physical Science Imaging Centre, Diamond Light Source Ltd., OX11 0DE, UK

Keywords: single atom catalysts, main-group metals, sulfur doping, oxygen reduction reaction, catalytic selectivity

Abstract: The selective oxygen reduction reaction (ORR) is important for various energy conversion processes such as the fuel cells and metal-air batteries for the $4e^-$ pathway and hydrogen peroxide (H_2O_2) electrosynthesis for the $2e^-$ pathway. However, it remains a challenge to tune the ORR selectivity of a catalyst in a controllable manner. Herein, we report an efficient strategy for introducing sulfur dopants to regulate the ORR selectivity of main-group Sb−N−C single-atom catalysts. Significantly, Sb−N−C with the highest sulfur content follows a $2e^-$ pathway with a high H_2O_2 selectivity (96.8%) and a remarkable mass activity (96.1 A g^{-1} at 0.65 V), while the sister catalyst with the lowest sulfur content directs a $4e^-$ pathway with a half-wave potential ($E_{1/2}$ = 0.89 V) that is more positive than commercial Pt/C. In addition, practical applications for these two $2e^-$/$4e^-$ ORR catalysts are demonstrated by

bulk H_2O_2 electrosynthesis for the degradation of organic pollutants and a high-power zinc-air battery, respectively. Combined experimental and theoretical studies reveals that the excellent selectivity for the sulfurized Sb−N−Cs is attributed to the optimal adsorption-desorption of the ORR intermediates realized through the electronic structure modulation by the sulfur dopants.

1. Introduction

Electrochemical oxygen reduction reaction (ORR) plays vital roles in renewable energy conversion and utilization[1]. It converts molecular oxygen (O_2) to water (H_2O) via the four-electron ($4e^-$) pathway or to hydrogen peroxide (H_2O_2) via the two-electron ($2e^-$) pathway[2]. The $4e^-$ ORR is critical to various energy conversion devices such as fuel cells and metal-air batteries that transform chemical energy directly into electricity[3]. On the other hand, the $2e^-$ ORR provides an environmentally safe and sustainable method for the production of H_2O_2, an important chemical that finds a wide range of applications in water disinfection, bleaching, energy carrier and so on[4]. The development of high-performance catalysts towards either the $4e^-$ or $2e^-$ ORR is the key for the processes to proceed at practical rates with high energy efficiencies. While noble metal-based electrocatalysts are both highly efficient for the $4e^-$ ORR (e.g., Pt, Pt-Co, Pt-Ni) and the $2e^-$ ORR (e.g., Pd-Au, Pt-Hg, Pd-Hg), the high cost and scarcity of noble metals impede their widespread employment[5]. Therefore, an increasing number of cost-effective electrocatalysts have been explored and some of them have displayed competitive catalytic performance to noble metals[6]. However, there are lacks of effective strategies to steer the ORR pathways in a controllable manner so as to generate either H_2O or H_2O_2 with both high selectivity and activity.

The ORR selectivity of a catalyst between the $2e^-$ and $4e^-$ pathway relies on the binding strength of the key intermediate *OOH on the active sites, which is further dictated by the electronic structure of the catalysts[7]. Thus, catalysts with tunable electronic structures are promising for the on-demand steering of the ORR pathways. In this regard, metal-nitrogen-carbon materials (M−N−Cs) with atomically dispersed M−N_x moieties, a unique subclass of single atom catalysts (SACs), provide great opportunities for tuning the ORR selectivity considering that their electronic structure is highly sensitive to the neighboring coordination environments that can be readily modified with high degrees of freedom[8]. For example, recent studies have demonstrated that regulating the first, second and even higher-coordination shells by introducing heteroatoms (e.g., O, B, S, P) into M−N−Cs is an effective strategy to engineer the electronic structure of the active sites[4b, 9]. However, the associated

efforts have been mainly focused on the *d*-block transition metal-based M−N−Cs (M = Fe, Co, Pt, etc.) to correlate the *d*-band center with the ORR selectivity[6a, 6b], while main group (*s*-block and *p*-block) metal-based M−N−Cs (M = Mg, Ca, In, Sb, etc.) with closed *d*-band shells are considerably underexplored.

In contrast to transition metal-based M−N−Cs, main group metal-based M−N−Cs can exhibit superior catalytic properties by engineering the $M-N_x$ moieties with partially occupied *p* orbitals of the metal sites, while providing additional benefits in terms of improved durability by mitigating the transition metal-induced Fenton reactions. For example, it was reported that the *p*-orbital electronic structure of Ca could be regulated by N and O coordination so that the highest peak of the projected density of states (PDOS) for the Ca atom is moved closer to the Fermi level, resulting in the enhanced adsorption of the ORR intermediates and higher activity towards the $4e^-$ ORR[10]. In another study, the lowest unoccupied molecular orbital of $In-N_x$ and the charge localization of the In center are tuned by S and B atoms in the first and second coordination spheres, thereby enhancing the binding energy of the *OOH intermediate at the In sites and optimizing the catalytic activity towards the $2e^-$ ORR[9b]. While the main-group M−N−Cs with *s*/*p*-electron activation have been demonstrated to be active and robust ORR electrocatalysts, previous studies were generally focused on modulating the activity of the catalysts and rarely mentioned about the regulation of the selectivity. Therefore, the exploration of strategies in controlling the ORR pathways of the main-group M−N−Cs and understanding the tuning mechanism is the key to developing high-performance main-group M−N−Cs for practical applications.

Herein, we prepared a series of main-group Sb−N−C catalysts with varied contents of sulfur dopants and tunable electronic structures that exhibit high ORR selectivity towards either the $4e^-$ ORR or the $2e^-$ ORR (Figure 1a). By carefully optimizing the processing conditions, three Sb−N−C catalysts with sulfur contents distributed in a wide range were prepared, including high-sulfur Sb−N−C (denoted as HS/Sb−N−C thereafter) (8.85 at%), medium-sulfur Sb−N−C (MS/Sb−N−C) (4.82 at%) and low-sulfur Sb−N−C (LS/Sb−N−C) (0.27 at%). The sulfurization degree is strongly correlated to the oxidation state of the $Sb^{\delta+}$ sites in HS/Sb−N−C (δ = ~1.0), MS/Sb−N−C (δ = ~1.5) and LS/Sb−N−C (δ = ~2.0). As a result of the varied sulfur contents and electronic structures, different behaviors in the ORR selectivity, manifested by the electron transfer number (*n*) and average H_2O_2 selectivity (H_2O_2%, 0.2 V – 0.7 V), are observed in HS/Sb−N−C (*n* = 2.14, H_2O_2% = 93.5%), MS/Sb−N−C (*n* = 3.32, H_2O_2% = 33.8%) and LS/Sb−N−C (*n* = 3.84, H_2O_2% = 8.4%).

Furthermore, HS/Sb−N−C shows a remarkable mass activity of 96.1 A g^{-1} (at 0.65 V) for the 2e⁻ ORR toward the electrosynthesis of H_2O_2 and when assembled into a H-cell electrolyzer it exhibits a high degradation efficiency (~99.7%) for the Fenton degradation of the representative dye pollutant rhodamine B (RhB). On the other hand, as a highly efficient catalyst for the 4e⁻ ORR, LS/Sb−N−C possesses a higher half-wave potential ($E_{1/2}$ = 0.89 V) than commercial Pt/C ($E_{1/2}$ = 0.86 V) and a small Tafel slope of 49.5 mV dec^{-1}, and it demonstrates a high power density of 295.1 mW cm^{-2} in a Zn-air battery. Density functional theory (DFT) calculations reveal that the binding strength of the key reaction intermediate *OOH in Sb−N−Cs is tuned by the sulfur dopants, accounting for the tuned ORR selectivity.

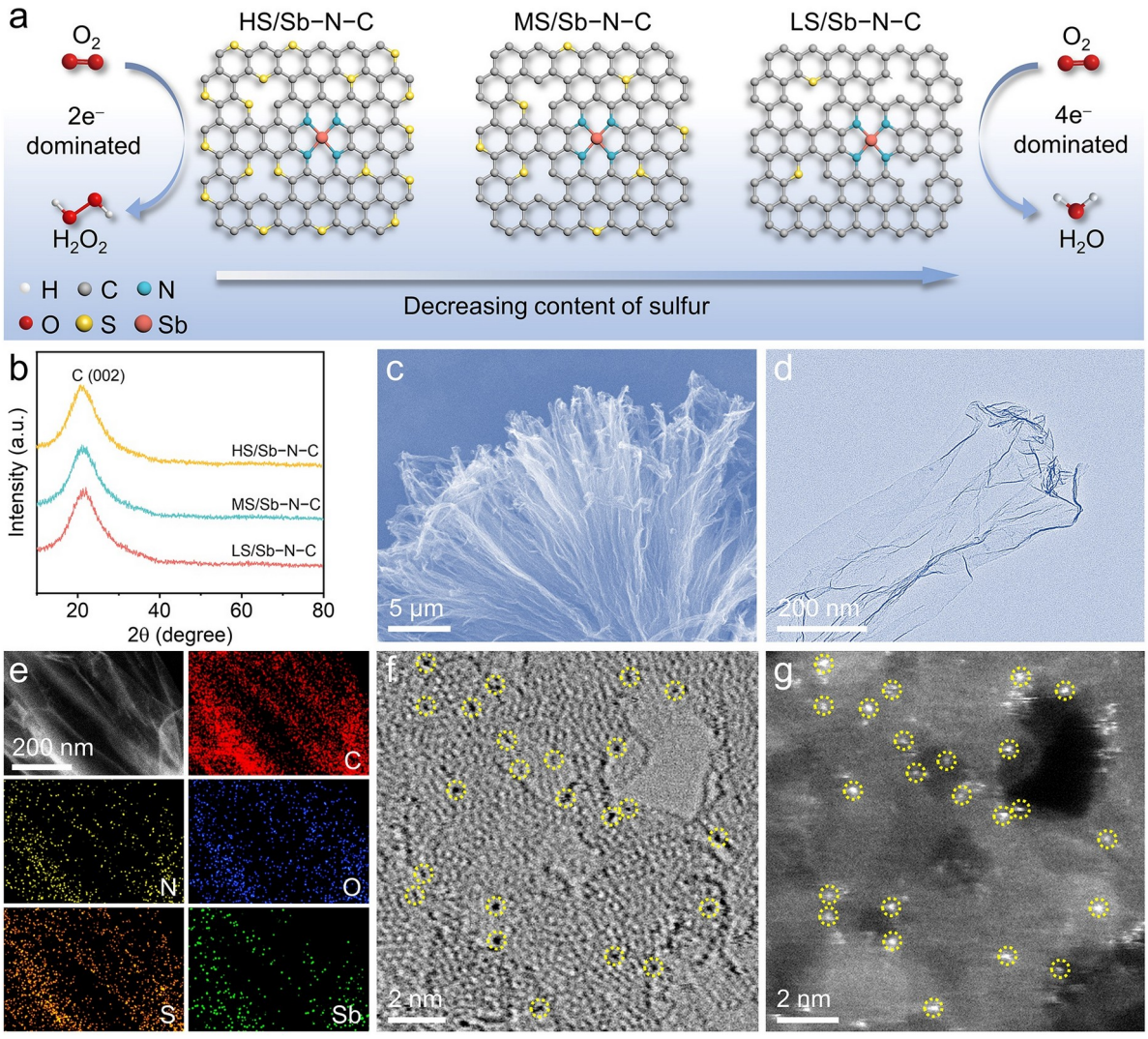

Figure 1. Synthesis and characterizations of Sb−N−Cs. a) Schematic structural models of HS/Sb−N−C, MS/Sb−N−C and LS/Sb−N−C towards the selective ORR electrocatalysis. b) XRD patterns of HS/Sb−N−C, MS/Sb−N−C and LS/Sb−N−C. c) SEM image, d) TEM image, e) EDS elemental mapping images, f) High-resolution bright-field STEM image and g) High-resolution dark-field STEM image of LS/Sb−N−C.

2. Results and Discussion

2.1. Synthesis and characterization of Sb−N−Cs

HS/Sb−N−C was prepared via a Sb_2S_3-templated method following our previous work[4c]. MS/Sb−N−C and LS/Sb−N−C were prepared by annealing HS/Sb−N−C at 600 °C and 800 °C, respectively, under Ar/NH_3 atmosphere to partially remove the sulfur dopants. It is noted that the calcination temperature has been optimized by evaluating the catalytic performances of samples calcinated at different temperatures (Figure S1, Supporting Information). The detailed description for the preparation of HS/Sb−N−C, MS/Sb−N−C, LS/Sb−N−C was provided in the Experimental Section. As shown in Figure 1b, X-ray powder diffraction (XRD) patterns of HS/Sb−N−C, MS/Sb−N−C and LS/Sb−N−C all display only a broad peak at ~23.6° assigned to the C (002) plane without the presence of characteristic peaks of Sb-derived crystallite[11]. Scanning electron microscopy (SEM) images reveal that these catalysts display similarly a flower-like architecture consisting of clusters of carbon nanofibers bunched at one end and splayed out at the other (Figure 1c and Figure S2, Supporting Information). Transmission electron microscopy (TEM) images unveil that the carbon nanofibers collapse together with crumples due to their flexible thin walls and hollow structures (Figure 1d and Figure S3, Supporting Information). Moreover, the surface of the carbon nanofibers is clean with no presence of metal particles, consistent with the XRD results. The energy-dispersive X-ray spectroscopy (EDS) elemental mapping reveals the uniform distribution of Sb, S, N, O, and C elements throughout the sample (Figure 1e). The high-resolution bright-field and dark-field scanning transmission electron microscopy (STEM) images suggest that the Sb metals are dispersed in the carbon matrix as individual atoms, represented by the dark dots in bright-field image and bright dots in the dark-field image, respectively (Figure 1f,g and Figure S4, Supporting Information). The nitrogen adsorption-desorption isotherms determine that HS/Sb−N−C, MS/Sb−N−C and LS/Sb−N−C has an increasing Brunauer-Emmett-Teller (BET) specific surface area of 433.6 $m^2\ g^{-1}$, 598.2 $m^2\ g^{-1}$ and 1146.9 $m^2\ g^{-1}$, respectively, and the corresponding pore size distributions reveal the formation of abundant mesopores and micropores with the removal of the sulfur dopants (Figure S5, Supporting Information)[12].

2.2. Analysis of atomic and electronic structure

The local coordination environment of Sb within the catalysts was firstly analyzed by Fourier-transform k^2-weighted extended X-ray absorption fine structure (FT-EXAFS) spectroscopy. As shown in Figure 2a, HS/Sb−N−C, MS/Sb−N−C and LS/Sb−N−C exhibit a

prominent peak at ~1.41 Å that can be assigned to the atomic Sb coordinated to light heteroatoms such as N, while no peak at ~2.71 Å associated with the Sb−Sb bond was observed, indicating the atomic dispersion of Sb. Wavelet-transform EXAFS (WT-EXAFS) of these catalysts display a strong signal in the contour plot at ~4.2 $Å^{-1}$(Figure S6, Supporting Information), distinctly different from the Sb foil (~8.2 $Å^{-1}$), confirming the atomic dispersion of Sb. The quantitative least-squares *R*-space and *k*-space EXAFS curve-fitting analysis was carried out to investigate the coordination configuration of Sb (Figure 2b, Figure S7 and Table S1, Supporting Information). The best fitting results for the first coordination shell determine that the coordination number of the Sb atom ~3.6, ~4.0 and ~4.1 in HS/Sb−N−C, MS/Sb−N−C and LS/Sb−N−C, respectively, suggesting the adoption of the $Sb-N_4$ configuration in them (inset in Figure 2b). The elemental compositions and chemical states of the catalysts were studied with X-ray photoelectron spectroscopy (XPS). As shown in Figure 2c, XPS survey spectra reveals the presence of Sb, S, N, O, and C elements in the three catalysts and one notable feature is the significantly different intensities in the sulfur peak. As summarized in Figure 2d and Table S2 (Supporting Information), HS/Sb−N−C has a higher sulfur content (8.85 at%) than MS/Sb−N−C (4.82 at%) and LS/Sb−N−C (0.27 at%). For the high-resolution S 2*p* XPS spectra (Figure 2e), the main sulfur species is C−S−C with minor contributions from the $-SO_x$ species. The presence of C−S−C could exert an electron-donating effect on the carbon substrate and thus modulate the electronic structure of the $M-N_x$ moieties[13]. The high-resolution C 1*s* and N 1*s* XPS profiles and the deconvoluted spectra of the three catalysts were displayed in Figure S8 and Figure S9 (Supporting Information), respectively. As shown in the Raman spectra (Figure 2f), the G band of LS/Sb−N−C is up-shifted to ~1592.5 cm^{-1}, compared to that of MS/Sb−N−C (~1562.5 cm^{-1}) and HS/Sb−N−C (~1552.5 cm^{-1}), indicating the electronic structure tuning of the carbon substrate by the C−S−C species[13a, 14]. The chemical oxidation state of the Sb species was analyzed by XPS and X-ray absorption near-edge structure (XANES). Deconvolutions of the Sb 3*d*/O 1*s* XPS spectra for the three catalysts show that the binding energy of the peaks assigned to the Sb $3d_{5/2}$ and Sb $3d_{3/2}$ are higher than those (528.6 eV and 538.0 eV) of Sb metals (Figure 2g), indicating that the Sb is in ionic state ($Sb^{\delta+}$)[15]. Moreover, the Sb 3*d* peaks shift to the higher binding energy from HS/Sb−N−C, MS/Sb−N−C to LS/Sb−N−C, indicating the higher oxidation state with the decrease in the sulfur content. From the Sb K-edge XANES spectra (Figure 2h), the Sb K-edge positions of the three catalysts are located between those of Sb foil and Sb_2O_3, suggesting that the oxidation states of Sb are between 0 and +3. Based on the linear fitting of the Sb K-edge position of XANES spectra for the three Sb−N−C catalysts and

the reference samples (Figure 2i and Figure S10, Supporting Information)[9b], the oxidation states of Sb for HS/Sb−N−C, MS/Sb−N−C and LS/Sb−N−C are determined to be ~1.0, ~1.5 and ~2.0, respectively.

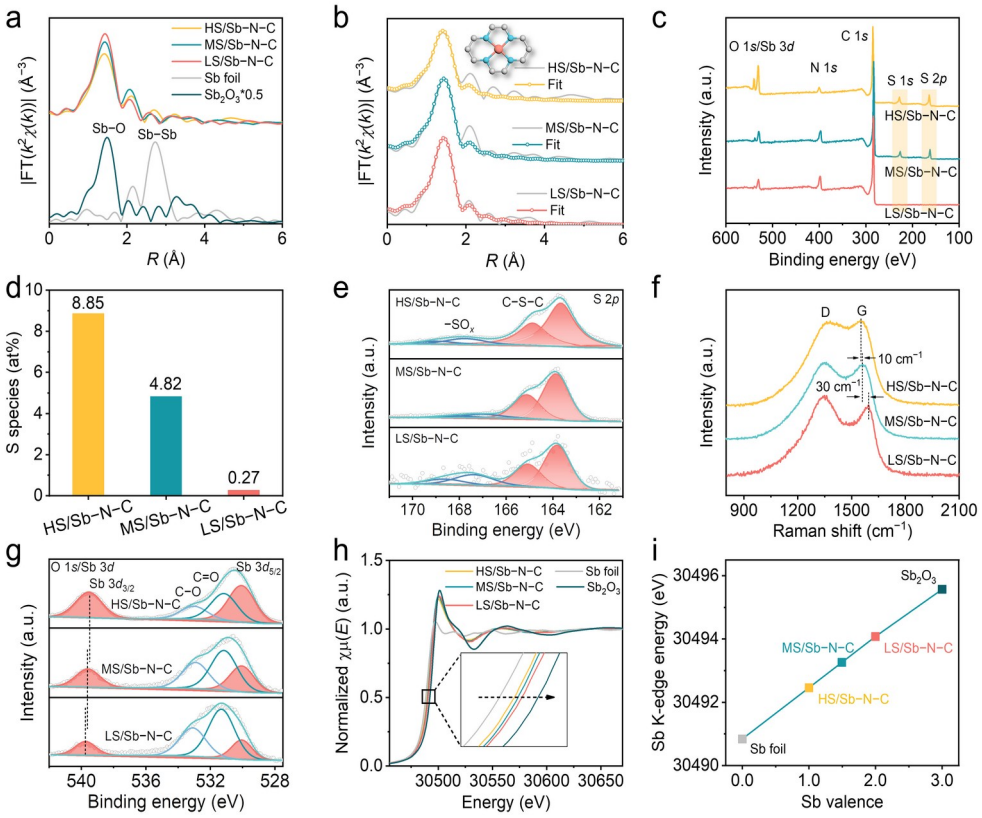

Figure 2. Atomic and electronic structure of Sb−N−Cs. a) The k^2-weighted FT-EXAFS spectra of different samples and b) FT-EXAFS fitting plots of HS/Sb−N−C, MS/Sb−N−C and LS/Sb−N−C. The inset in (b) is the structural model of the Sb−N_4 moiety. c) XPS survey spectrum of HS/Sb−N−C, MS/Sb−N−C and LS/Sb−N−C. d) Chart showing the atomic percentages of sulfur species in HS/Sb−N−C, MS/Sb−N−C and LS/Sb−N−C determined by XPS. e) High-resolution XPS spectrum of S 2*p*. f) Raman spectra of HS/Sb−N−C, MS/Sb−N−C and LS/Sb−N−C. g) High-resolution XPS spectrum of Sb 3*d*/O 1*s*. h) The Sb K-edge XANES spectra of different samples. i) Linear fitting curve of Sb−N−Cs and references derived from the corresponding Sb K-edge energy position of XANES spectra.

2.3. Electrocatalytic ORR performance

The ORR measurements were performed in O_2-saturated 0.1 M KOH solution using the three-electrode system with the rotating ring-disk electrode (RRDE) as the working electrode.

The catalysts loading was optimized and the results were provided in Figure S11, Supporting Information. The collection efficiency (*N*) of the RRDE was determined to be 0.365 (Figure S12, Supporting Information). All potentials were converted to a reversible hydrogen electrode (RHE) based on the calibration result (Figure S13, Supporting Information). Figure 3a shows the linear sweep voltammetry (LSV) curves for the ORR collected at 1600 rpm, together with the H_2O_2 oxidation current density collected at the Pt ring electrode poised at a constant potential of 1.20 V versus RHE. It is apparent that the ring current density decreases in the order HS/Sb−N−C > MS/Sb−N−C > LS/Sb−N−C while the disk current density shows an increasing trend, indicating that the $2e^-$ pathway is converted to the $4e^-$ pathway with the content of sulfur decreasing. The calculated H_2O_2 selectivity (%) and electron transfer number (*n*) as a function of potential from the RRDE measurements were plotted in Figure 3b. The results show that HS/Sb−N−C possesses a high average H_2O_2 selectivity from 0.2 V – 0.7 V of ~93.5% and a low *n* value of 2.14, highlighting that it directs a highly selective $2e^-$ ORR pathway. For MS/Sb−N−C, its H_2O_2 selectivity is ~33.8% and the *n* value is 3.32. For LS/Sb−N−C, it presents a much lower H_2O_2 selectivity of ~8.4% and higher *n* value of 3.84, indicating that the ORR follows the $4e^-$ pathway. The *n* value for the ORR was further calculated from the Koutecký-Levich (K-L) plots derived from the LSV curves at different rotation speeds (Figure 3c and Figure S14, Supporting Information). HS/Sb−N−C, MS/Sb−N−C and LS/Sb−N−C show an increased *n* value in the order of ~2.6 < ~3.2 < ~4.0, confirming that the ORR was steered from the $2e^-$ pathway to the $4e^-$ pathway with the sulfur content decreasing. Remarkably, HS/Sb−N−C with a high H_2O_2 selectivity (maximized at 96.8%) and mass activity (96.1 A g^{-1} at 0.65 V) towards the $2e^-$ ORR is superior to almost all the previously reported M−N−Cs (Figure 3d and Table S3, Supporting Information). H_2O_2 reduction reaction measurements suggest that HS/Sb−N−C exhibited much lower H_2O_2 reduction currents compared to MS/Sb−N−C, LS/Sb−N−C and Pt/C (Figure S15, Supporting Information), which could avoid the further reduction of the H_2O_2 product[16]. Moreover, HS/Sb−N−C shows stable activity and selectivity, as demonstrated by the 10-h chronoamperometry test (Figure S16, Supporting Information). LS/Sb−N−C with a high half-wave potential ($E_{1/2}$ = 0.89 V) and small Tafel slope (49.5 mV dec^{-1}) towards the $4e^-$ ORR is superior to the commercial Pt/C ($E_{1/2}$ = 0.86 V, Tafel slope = 70.5 mV dec^{-1}), making it among the best main-group metal-based M−N−Cs (Figure 3e, Figure S17 and Table S4, Supporting Information). Meanwhile, LS/Sb−N−C shows high durability, as evidenced by the 5000 scans of cyclic voltammetry (CV) and 12-h chronoamperometry test (Figure S18, Supporting Information).

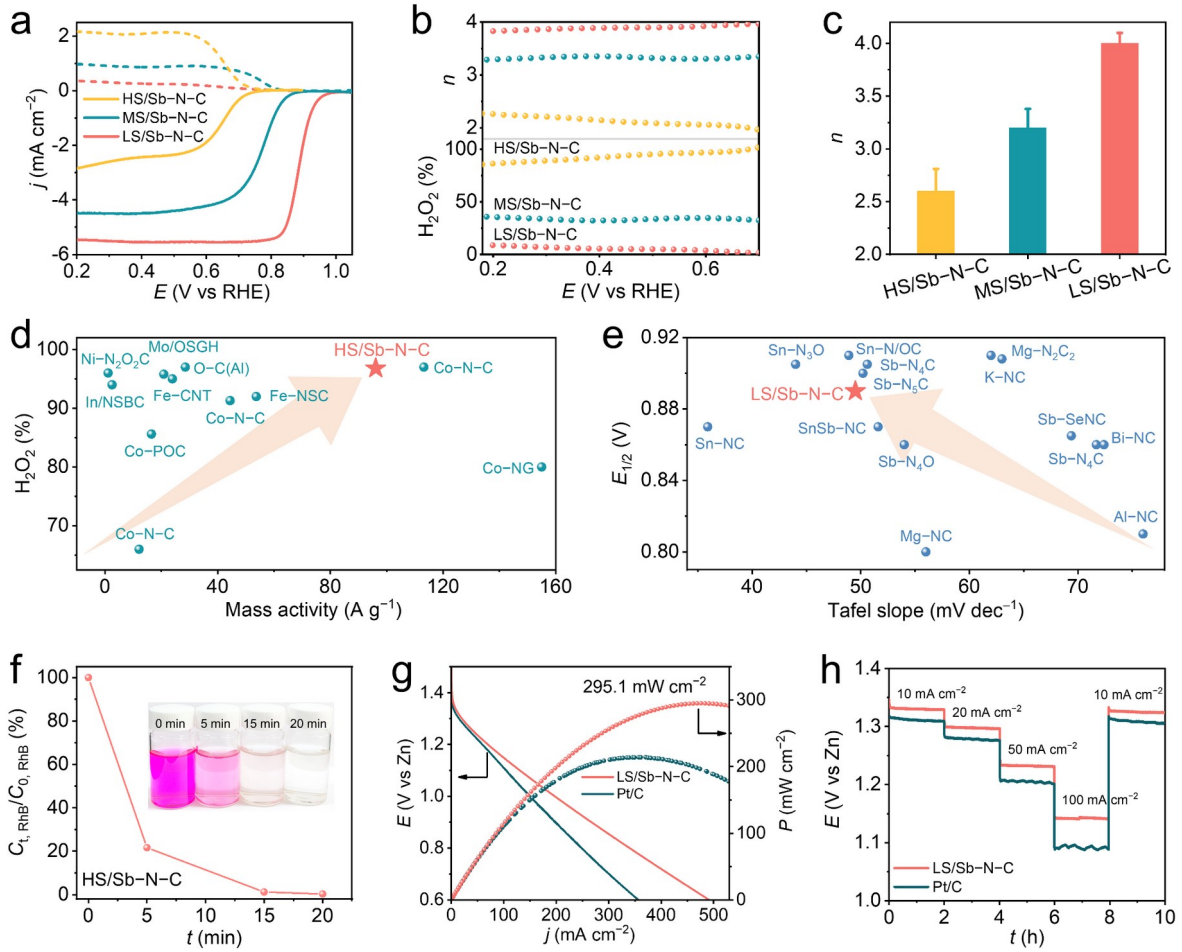

Figure 3. Electrocatalytic ORR performance. a) ORR polarization curves (solid lines) at a rotation of 1600 rpm and simultaneous H_2O_2 detection currents on the ring electrode (dashed lines) for HS/Sb−N−C, MS/Sb−N−C and LS/Sb−N−C in O_2-saturated 0.1 M KOH electrolyte. The catalyst loadings are 20.2 μg cm^{-2}, 80.8 μg cm^{-2} and 161.6 μg cm^{-2} for HS/Sb−N−C, MS/Sb−N−C and LS/Sb−N−C, respectively. b) Calculated H_2O_2 selectivity (%) and electron transfer number (*n*) based on the RRDE measurements. c) Chart showing the electron transfer number (*n*) based on the K-L plots. d) Comparison of the maximum H_2O_2 selectivity and mass activity at 0.65 V toward H_2O_2 production on HS/Sb−N−C in alkaline media with previously reported M−N−Cs in Table S3, Supporting Information. e) Comparison of the half-wave potential ($E_{1/2}$) and Tafel slope for the 4e$^-$ ORR in alkaline media between LS/Sb−N−C and previously reported main-group metal-based M−N−Cs in Table S4, Supporting Information. f) The degradation efficiency of organic dye RhB over time. The inset shows the photos of the RhB solution after adding catholyte during the degradation process. g) The discharge polarization curves and the corresponding power densities of LS/Sb−N−C and commercial Pt/C in a Zn-air battery. h) The discharge platforms of LS/Sb−N−C and Pt/C at various current densities in a Zn-air battery.

Inspired by the high performance of HS/Sb−N−C for the 2e⁻ ORR and LS/Sb−N−C for the 4e⁻ ORR, devices were fabricated to demonstrate their uses in practical applications. For HS/Sb−N−C, it was casted on a hydrophobic carbon fiber paper for the bulk electrosynthesis of H_2O_2 in an H-cell electrolyzer containing O_2-saturated 0.1 M KOH solution (Figure S19, Supporting Information). To determine the Faradaic efficiency of HS/Sb−N−C, the potentials of the working electrode were kept constant for 200 s at each selected value and the accumulated amounts of H_2O_2 in the electrolyte of the cathode compartment were determined by a colorimetric quantification method (Figure S20, Supporting Information). The Faradaic efficiency of HS/Sb−N−C for H_2O_2 generation is between 88.6% and 96.3% in the wide potential range of 0.20 – 0.70 V. Moreover, during the bulk electrolysis at 0.5 V, HS/Sb−N−C exhibited a high production rate of 5.04 mol $g_{catalyst}^{-1}$ h^{-1} and the current density of ~10 mA cm^{-2} maintained for 10 h without noticeable degradation, enabling a continuous and stable production of H_2O_2, suggesting its potential for practical applications. The catholyte after electrolysis was employed for the degradation of organic dye RhB to mimic wastewater treatment via the Fenton reaction and the evaluation in the concentration of RhB was monitored by UV-vis spectrophotometry. As shown in Figure 3f, after adding 2.0 mL of the catholyte collected at the cathode compartment with the working electrode kept at a constant potential of 0.4 V for 20 min, the fresh RhB solution (10 mL, 10 mg L^{-1}) was completely degraded (degradation efficiency of ~99.7%) to be colorless (inset in Figure 3f). For LS/Sb−N−C, it was utilized in a stack-type Zn-air battery with a polished Zn plate as the anode and the carbon paper coated with LS/Sb−N−C as the air cathode (Figure S21, Supporting Information). The open-circuit voltage of the as-fabricated Zn-air battery is 1.57 V, which is higher than that of Pt/C (1.44 V) and close to the thermodynamic value (1.65 V) (Figure S22, Supporting Information). Figure 3g displays the discharge curves of LS/Sb−N−C and Pt/C, showing that the peak power density of LS/Sb−N−C is up to 295.1 mW cm^{-2}, significantly higher than that of Pt/C (214.2 mW cm^{-2}). LS/Sb−N−C delivers a specific capacity of 814.3 mAh g_{Zn}^{-1}, higher than that of Pt/C (807.4 mAh g_{Zn}^{-1}) and close to the theoretical capacity of 820 mAh g_{Zn}^{-1} (Figure S23, Supporting Information). Furthermore, the rate capability for the batteries was evaluated by operating them at different current densities from 10 mA cm^{-2} to 100 mA cm^{-2}. As shown in Figure 3h, LS/Sb−N−C exhibits a higher voltage platform than Pt/C at the same discharge current density. Besides, the voltage could recover to 1.33 V when the current density was switched back to 10 mA cm^{-2}, indicating good rate capability and durability of LS/Sb−N−C. These results suggest that the Sb−N−C catalysts

with the tunable ORR selectivity are promising candidates for different types of practical applications.

2.4. Theoretical calculations

To gain insights into the effect of the sulfur contents on the ORR pathway, density functional theory (DFT) calculations were performed to simulate both the $4e^-$and $2e^-$ reaction pathways of the ORR. Figure 4a shows the optimized structures of the LS/Sb−N−C and HS/Sb−N−C models. The optimized geometries for the structures of all possible intermediates adsorbed on LS/Sb−N−C and HS/Sb−N−C are presented in Figure S24, Supporting Information. The Sb sites with *OOH adsorbed in LS/Sb−N−C and HS/Sb−N−C were first studied since the adsorption strength of *OOH is generally regarded as a suitable descriptor for governing the ORR selectivity of the catalysts[5d]. Figure 4b shows the differences in the electron density distributions on LS/Sb−N−C and HS/Sb−N−C with *OOH adsorbed. Compared with LS/Sb−N−C, HS/Sb−N−C exhibits a more pronounced electron transfer from the $Sb-N_4$ site to the *OOH intermediate. This suggests that the additional charge could potentially occupy the anti-bounding orbitals of the *OOH intermediate, resulting in diminished absorption of the *OOH intermediate. Furthermore, as shown in Figure 4c, the *OOH adsorption energy (ΔG_{*OOH}) on LS/Sb−N−C is 3.71 eV, which is considerably closer to the optimum for the $4e^-$ ORR pathway of 3.90 eV. Instead, the ΔG_{*OOH} of HS/Sb−N−C is 4.04 eV, which is much closer to the optimum for the $2e^-$ ORR (4.22 eV). To gain further insights into the catalytic selectivity, the free energy diagrams of the $4e^-/2e^-$ ORR pathway intermediates on LS/Sb−N−C and HS/Sb−N−C under the applied potentials of 1.23 V and 0.68 V were calculated and displayed in Figure 4d and Figure 4e, respectively. For the $4e^-$ ORR pathway, LS/Sb−N−C has a lower ΔG value (0.038 eV) for the *OOH formation than that of HS/Sb−N−C (0.354 eV), indicating that the $4e^-$ ORR pathway is energetically favored on LS/Sb−N−C. For the $2e^-$ ORR pathway, HS/Sb−N−C exhibits a smaller ΔG (0.195 eV) for the removal of the *OOH to form H_2O_2 than that of LS/Sb−N−C (0.512 eV), suggesting that the $2e^-$ ORR pathway is preferred over the HS/Sb−N−C. These mechanical studies suggest that the selectivity of the $Sb-N_4$ moieties towards the $4e^-/2e^-$ ORR pathway could be tuned by the content of sulfur dopants, corroborating the experimental observations.

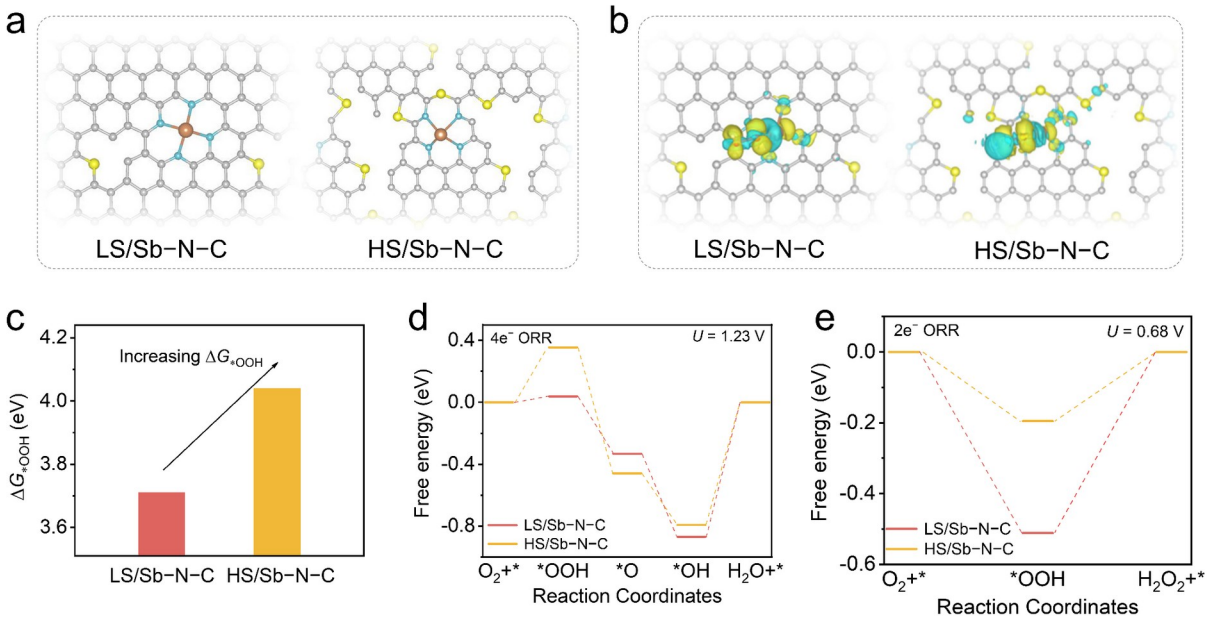

Figure 4. Theoretical calculations. a) Top views of the optimized structural models of LS/Sb−N−C and HS/Sb−N−C. The gray, blue, yellow, and purple spheres represent C, N, S, and Sb atoms, respectively. b) The calculated electron density distribution for the corresponding structural models in (a) with *OOH adsorbed. The yellow and cyan represent the electron gain and loss, respectively. c) Calculated *OOH adsorption energies on the Sb center in LS/Sb−N−C and HS/Sb−N−C. Free energy profiles of d) $4e^-$ ORR pathway under the electrode potential of 1.23 V and e) $2e^-$ ORR pathway under the potential of 0.68 V on LS/Sb−N−C and HS/Sb−N−C, respectively.

3. Conclusion

In summary, we have constructed a series of main-group Sb−N−C catalysts with varied contents of sulfur dopants in the carbon support. The electronic structure and oxidation state of the atomic Sb centers are strongly correlated to the sulfur contents in Sb−N−Cs. These sulfurized Sb−N−C catalysts exhibit tunable selectivity towards either the $2e^-$ ORR or the $4e^-$ ORR depending on the sulfur contents. In particular, HS/Sb−N−C with the highest sulfur content exhibits a superior $2e^-$ ORR performance than most previously reported SACs in alkaline media, with a high selectivity (maximized at 96.8%) and mass activity (96.1 A g^{-1} at 0.65 V), and when assembled into a H-cell electrolyzer towards the bulk H_2O_2 electrosynthesis it exhibits a high degradation efficiency (~99.7%) for the Fenton degradation of the representative dye pollutant RhB. In addition, LS/Sb−N−C with the lowest sulfur content presents a high performance towards the $4e^-$ ORR with a half-wave potential of 0.89 V and a small Tafel slope of 49.5 mV dec^{-1}, and it demonstrates a high power density of 295.1 mW cm^{-2} in a Zn-air battery. This work provides an effective strategy to regulate the

electronic structure of M−N−Cs for the on-demand optimization of their catalytic selectivity and pave the way for the development of high-performance main-group M−N−Cs for practical electrocatalytic applications.

4. Experimental Section/Methods

Materials: Antimony acetate ($C_6H_9O_6Sb$), thioacetamide (C_2H_5NS) and ethylene glycol ($(CH_2OH)_2$) were purchased from Shanghai Macklin Biochemical Co., Ltd. Rhodamine B (RhB, 95%), Nafion 117 solution (5 wt%) and other chemicals were purchased from Sigma-Aldrich. Hydrophobic carbon fiber paper was purchased from Shanghai Hesen. All the chemicals were directly purchased without further processing and the ultrapure water used in the experiments has a resistivity of 18.25 MΩ cm^{-1}.

Preparation of HS/Sb−N−C. Firstly, 30.0 g of thioacetamide and 30.0 g of antimony acetate were dissolved in 30 mL of ethylene glycol and the mixture was stirred for 24 h to form a red homogeneous suspension. The obtained suspension was transferred into a porcelain boat and annealed in a tube furnace at 500 °C for 5 h with a ramping rate of 3 °C min^{-1} under N_2 atmosphere. After that, the sample was treated with a secondary annealing at 600 °C for 2 h with a ramping rate of 3 °C min^{-1} under vacuum (~60.0 Pa) to obtain HS/Sb−N−C.

Preparation of MS/Sb−N−C. MS/Sb−N−C was prepared by annealing HS/Sb−N−C in a tube furnace at 600 °C for 1 h with a ramping rate of 20 °C min^{-1} under Ar (150 sccm) and NH_3 (50 sccm) atmosphere to partially remove the sulfur dopants.

Preparation of LS/Sb−N−C. LS/Sb−N−C was prepared with the same process as that of MS/Sb−N−C except that the annealing process was performed at 800 °C for 1 h to remove more sulfur dopants.

Material Characterizations. SEM was conducted on a Plus Sigma ZEISS operated at 2 kV. TEM was carried out on a JEOL JEM-2100Plus microscope operated at an accelerating voltage of 200 kV and a Thermo Scientific Themis Z (3.2) operated at an accelerating voltage of 300 kV. XRD analyses were carried out on a Bruker D8 Advance diffractometer with Cu Kα radiation (λ ≈ 1.54 Å). Raman spectra were recorded on a Thermo Scientific DXR Raman microscope with a 532 nm laser. XPS spectra were collected using a Thermo Scientific ESCALAB 250Xi system with Al Kα radiation ($h\nu$ = 1486.6 eV). ADF-STEM was performed on a JEOL ARM300 CF with JEOL ETA aberration correctors with a beam energy of 80 keV and a 40 mm condenser lens aperture (32 mrad), an ADF detector (inner angle 47 mrad), and a beam current of approximately 46 pA. The Sb K-edge X-ray absorption spectra were

performed with a Si (311) crystal monochromator at BL14W1 beamline of Shanghai Synchrotron Radiation Facility (SSRF). The storage ring energy was operated at 3.5 GeV with a ring current of 130 to 210 mA. The data analysis for the X-ray absorption spectroscopy using IFEFFIT was conducted using the Demeter system.

Electrochemical Measurements. The electrochemical ORR performances of the catalysts were measured on a three-electrode cell equipped with a CHI 760E electrochemical workstation and a rotating ring disk electrode (RRDE) (Pine Research Instrumentation, USA). A graphite rod was used as the counter electrode and a Hg/HgO reference electrode filled with 1 M KOH was used for the measurements in the 0.1 M KOH electrolyte. The potential was converted to the RHE scale by $E_{RHE} = E_{Hg/HgO} + 0.895$ V based on the calibration results (Figure S13, Supporting Information). The RRDE with an electrode area of 0.2475 cm^2 was used as the working electrode. The ring collection efficiency (N) of RRDE was determined to be 0.365 using a typical redox couple of potassium ferricyanide solution (Figure S12, Supporting Information). To prepare the working electrode, 2.0 mg of catalyst and 20 µL Nafion (5 wt%) solution were mixed with 1.98 mL ethanol and then were dispersed by sonicating for 30 min to obtain a homogeneous ink. After polishing RRDE mechanically with alumina suspension, the prepared catalyst ink was drop-casted onto the disk electrode of RRDE and then the electrode was dried at room temperature to give a uniform catalyst layer. The catalysts loadings were optimized (Figure S11, Supporting Information), revealing that the optimal loadings are 20.2 µg cm^{-2}, 80.8 µg cm^{-2} and 161.6 µg cm^{-2} for HS/Sb−N−C, MS/Sb−N−C and LS/Sb−N−C, respectively. Before the ORR measurement, the pre-activation process by scanning cycle voltammetry (CV) curves at a rate of 50 mV s^{-1} from 0 V to 1.2 V was performed on RRDE to electrochemically clean it until stable state was obtained. Then, Pt ring was electrochemically cleaned from 0 V to −0.3 V for 40 cycles at a scan rate of 100 mV s^{-1}. Subsequently, the ORR polarization curves were obtained by linear sweep voltammograms (LSV) measurement with the sweep speed of 10 mV s^{-1} from 1.1 V to 0 V at 1600 rpm in O_2-saturated electrolyte, and the Pt ring electrode potential was maintained at 1.2 V to quantify the amounts of H_2O_2 produced on the disk electrode. The LSV curves were corrected with 95% *iR*-compensation and background non-Faradaic currents that were obtained by conducting the measurements in the N_2-saturated electrolyte. The H_2O_2 selectivity and the electron transfer number (n) were calculated based on the disk current (I_D) and ring current (I_{Ring}) data using the following equation:

$$H_2O_2 \text{ selectivity (\%)} = 200 \times \frac{\frac{I_R}{N}}{|I_D| + \frac{I_R}{N}} \quad (1)$$

$$n = 4 \times \frac{|I_D|}{|I_D| + \frac{I_R}{N}} \quad (2)$$

The Koutecký-Levich (K-L) plots can be obtained by scanning LSV at various rotating speeds. The electron transfer number (*n*) can be calculated from the K-L equation:

$$\frac{1}{j} = \frac{1}{j_l} + \frac{1}{j_k} = \frac{1}{B\omega^{1/2}} + \frac{1}{j_k} \quad (3)$$

$$B = 0.62nFC_0D^{2/3}V^{-1/6} \quad (4)$$

where j is the measured current density, j_k and j_l are the kinetic and diffusion-limited current densities, ω is the angular velocity of the disk, n is the electron transfer number, F is the Faraday constant (96485 C mol^{-1}), C_0 is the bulk concentration of O_2 (1.2×10^{-6} mol cm^{-3}), D is the diffusion coefficient of O_2 in 0.1 M KOH (1.9×10^{-5} cm^2 s^{-1}), and V is the kinematic viscosity of the 0.1 M KOH (0.011 cm^2 s^{-1}). The mass activity of HS/Sb−N−C toward the $2e^-$ ORR was calculated via dividing the kinetic current density at the ring electrode by the catalyst loading. For LS/Sb−N−C, the mass activity toward the $4e^-$ ORR was calculated via dividing the kinetic current density at the disk electrode by the catalyst loading. To analyze the kinetics of the catalysts, the Tafel plots were generated according to the equation:

$$E = a + b \times \log(j_k) \quad (5)$$

where a, E, j_k, and b are the constant, applied potential, kinetic current and Tafel slope, respectively.

Degradation experiment of organic dyes. The pollutant degradation measurements were performed with the solution of 10 mg L^{-1} RhB organic dye as the simulated wastewater. Before test, RhB was dissolved in DI water at various concentration and the calibration curves between absorbance and concentration of RhB were determined by measuring the absorbance at 554 nm through the UV-vis spectrophotometry, as shown in Figure S25, Supporting Information. The H_2O_2 was generated in a two compartment H-cell with anion exchange membrane as the separator. The cathode and anode compartments were filled with the same volume (30 mL) of 0.1 M KOH solution and the cathode electrolyte was saturated with O_2 by continuous bubbling. The working electrode was a hydrophobic carbon paper (1 cm^2, Hesen, HCP-120) with a HS/Sb−N−C loading of 0.1 mg cm^{-2}. A Hg/HgO electrode was utilized as

the reference electrode and platinum mesh as the counter electrode. The H_2O_2 concentration was measured by a traditional cerium sulfate ($Ce(SO_4)_2$) titration method based on the mechanism that a yellow solution of Ce^{4+} would be reduced by H_2O_2 to colorless Ce^{3+} ($2Ce^{4+} + H_2O_2 \rightarrow 2Ce^{3+} + 2H^+ + O_2$) to calculate the Faradaic efficiency for H_2O_2 generation. The concentrations of Ce^{4+} before and after the reaction were measured by the ultraviolet-visible spectroscopy. Standard $Ce(SO_4)_2$ solution (0.5 mM) was prepared by dissolving $Ce(SO_4)_2$ salts into 0.5 M sulfuric acid solution. The calibration curves between absorbance and Ce^{4+} concentration were determined by measuring the absorbance at 317 nm of different $Ce(SO_4)_2$ solutions with known concentrations (0.1 – 0.5 mM) (Figure S20, Supporting Information). After electrolysis for 200 s, 200 μL of the electrolyte in the cathode chamber after neutralization by 0.5 M sulfuric acid solution was added into the standard $Ce(SO_4)_2$ titrant solution. Based on the linear relationship between the signal intensity and Ce^{4+} concentration, the molar amounts of consumed Ce^{4+} after reaction could be obtained. By this approach, the amounts of H_2O_2 produced can be calculated as half the molar amounts of the Ce^{4+} consumed. The Faradaic efficiency was calculated by the following equation:

$$FE\ (\%) = 2 \times \frac{CVF}{Q} \tag{6}$$

where F is the Faraday constant (96485 C mol^{-1}), C is the concentration of H_2O_2, V is the volume of electrolyte and Q is the total charge during the ORR. After electrolysis at a constant potential of 0.4 V for a period of time (0 − 20 min), 2.0 mL of the catholyte was collected and acidified by 1.0 mL of 0.5 M H_2SO_4 containing 1 mM Fe^{2+} to produce strong oxidants via Fenton-reaction. Subsequently, 10 mL of the standard RhB solution (10 mg L^{-1}) was quickly added to the above strong oxidizing solution and shaken briefly. After that, the above mixture was measured through the UV-vis spectrophotometry (Figure S26, Supporting Information). The degradation efficiency of the RhB can be calculated as follows:

$$\frac{C_{t,RhB}}{C_{0,RhB}} = \frac{A_t - A_0}{A_0} \times 100 \tag{7}$$

where $C_{0,\ RhB}$ and $C_{t,\ RhB}$ are the RhB concentration (mg L^{-1}) at the initial time and degraded after a period of time, A_0 and A_t are the absorbance at the initial time and degraded after a period of time, respectively.

Zn-air battery tests. A stack-type Zn-air battery was assembled and tested under the following procedure. A polished Zn plate and 6 M KOH aqueous solution were used as anode and electrolyte, respectively. To prepare the air cathode, LS/Sb−N−C or commercial 20 wt% Pt/C ink was dropped onto the hydrophobic carbon paper with a loading of 0.4 mg cm^{-2}, and then

dried naturally. The discharge curves were tested on CHI 760E electrochemical workstation with a scanning rate of 10 mV s^{-1}. The specific capacity and the rate capability were tested on LANBTS System. The power density (P) is calculated based on the discharge current density (I) and the corresponding voltage (V) by the equation:

$$P = IV \tag{8}$$

The specific capacity (C_{sp}) is calculated as follows:

$$C_{sp} = It / m_{Zn} \tag{9}$$

where I is the discharge current density, t is the discharge time, and m_{Zn} is the mass of consumed Zn.

Calculation methods. The ab initio quantum mechanical (QM) calculations were performed using the Vienna Ab initio Simulation Package (VASP) at a version of 5.4.4 with the projector augmented wave (PAW) method and a plane wave basis set. Density functional theory (DFT) with generalized gradient approximation (GGA) was used for the Perdew-Burke-Ernzerhof (PBE) functional[17]. A dispersion correction, the DFT-D3 method with Becke-Jonson damping[18], was included in the calculations. The energy cutoff was set to 400 eV. A larger energy cutoff does not produce more accurate predictions based on our benchmark calculations. The reciprocal space was sampled by the Γ-centered Monkhorst-Pack scheme with a grid of 3×3×1 grid. A finer K spacing does not produce a more accurate prediction based on our benchmark calculation. The partial occupancies for each orbital are set with the first order Methfessel-Paxton scheme at a smearing width of 0.2 eV. The dipole moment corrections for the total energy are considered in the direction normal to the surface. The self-consistent electronic step is considered to converge when the changes in the total energy and the eigenvalues change between the two steps are both smaller than $1e^{-6}$ eV. A conjugate-gradient algorithm is used to relax the ions in energy minimization. The minimization was considered converged when all the atomic forces were are smaller than 0.01 eV/Å, where convergence to an energy minimum was confirmed in all cases with frequency calculations to verify that all imaginary frequencies were eliminated. The frequencies and normal modes are determined from the Hessian matrix. To calculate the Hessian matrix, finite differences are used. Each ion is displaced by ±0.04 Å in the direction of each Cartesian coordinate, and from the forces the Hessian matrix is determined. Only the adsorbed species are populated in the frequency calculation, while the slab atoms are kept fixed. The temperature is 298 K, and the pressure is 1 bar. The free energies for all the structures were computed using standard statistical mechanics formulas that account for translational,

rotational, vibrational, and electronic degrees of freedom[19]. Translational and rotational contributions to the free energy were omitted for all surface adsorbed species. The partition function under the harmonic oscillator approximation is as follows:

$$q_{vib} = \prod_i \frac{e^{-h\nu_i/2kT}}{1 - e^{-h\nu_i/kT}} \tag{10}$$

where k is a force constant and ν is the vibrational frequency. After substituting the partition function q_{vib}, the internal energy correction is as follows:

$$U_{vib}(T) = R\sum_i \left(\frac{h\nu_i}{k}\right)\left(\frac{1}{2} + \frac{e^{\frac{-h\nu_i}{kT}}}{1 - e^{\frac{-h\nu_i}{kT}}}\right) \tag{11}$$

The first term is the contribution of zero-point energy (ZPE), and the second term is the contribution of internal energy correction from 0 K to 298 K. The correction of entropy (S) is as follows:

$$S_{vib}(T) = R\sum_i \left\{\frac{h\nu_i}{kT}\frac{e^{\frac{-h\nu_i}{kT}}}{1 - e^{\frac{-h\nu_i}{kT}}} - \ln\left[1 - e^{\frac{-h\nu_i}{kT}}\right]\right\} \tag{12}$$

Here, the first term exactly cancels with the second term of the internal energy shown above. Therefore, only the second term of the entropy needs to be corrected. For adsorbed species, the six degrees of freedom of the translation and rotation are frustrated and considered vibrations. This approximation fails when the vibration is extremely low, which significantly contributes to the correction. To avoid such overestimation, the contributions of frequencies below 50 cm^{-1} are all considered to be 50 cm^{-1}.

The zero-point energy (ZPE) in thermoenergy correction is as follows:

$$\varepsilon_{ZPE} = \frac{h\nu}{2} \tag{13}$$

Adsorption mechanisms of *OOH, *O, and *OH intermediates were investigated in each model, which was optimized for convergence. For the ORR process, the Gibbs free energy G can be derived as follows:

$$G = E_{ZPE} + E + k_B T - TS \tag{14}$$

The above correction is obtained by using the VASPKIT code for postprocessing of the VASP calculated data[20].

Supporting Information

Supporting Information is available from the Wiley Online Library or from the author.

Acknowledgements

M. Yan and H. Yang contributed equally to this work. H.F. acknowledges financial support from the National Natural Science Foundation of China (grant no. 92163116) and Major Program of the Natural Science Foundation of Hunan Province (grant no. 2021JC0006). T. C. thanks the support from the National Natural Science Foundation of China (grant no. 22173066), the Natural Science Foundation of Jiangsu Province (grant no. BK20230065). This work was partly supported by the Collaborative Innovation Center of Suzhou Nano Science & Technology, the 111 Project, Joint International Research Laboratory of Carbon-Based Functional Materials and Devices.

Received: ((will be filled in by the editorial staff))
Revised: ((will be filled in by the editorial staff))
Published online: ((will be filled in by the editorial staff))

References

[1] I. Katsounaros, S. Cherevko, A. R. Zeradjanin, K. J. J. Mayrhofer, *Angew. Chem. Int. Ed.* **2014**, *53*, 102.

[2] J. Liu, Z. Gong, M. Yan, G. He, H. Gong, G. Ye, H. Fei, *Small* **2022**, *18*, 2103824.

[3] a) J. Liu, Z. Gong, C. Allen, W. Ge, H. Gong, J. Liao, J. Liu, K. Huang, M. Yan, R. Liu, G. He, J. Dong, G. Ye, H. Fei, *Chem Catal.* **2021**, *1*, 1291; b) K. Jiao, J. Xuan, Q. Du, Z. Bao, B. Xie, B. Wang, Y. Zhao, L. Fan, H. Wang, Z. Hou, S. Huo, N. P. Brandon, Y. Yin, M. D. Guiver, *Nature* **2021**, *595*, 361; c) Q. Zhang, S. Dong, P. Shao, Y. Zhu, Z. Mu, D. Sheng, T. Zhang, X. Jiang, R. Shao, Z. Ren, J. Xie, X. Feng, B. Wang, *Science* **2022**, *378*, 181.

[4] a) J. Tang, T. Zhao, D. Solanki, X. Miao, W. Zhou, S. Hu, *Joule* **2021**, *5*, 1432; b) J. Liu, Z. Wei, Z. Gong, M. Yan, Y. Hu, S. Zhao, G. Ye, H. Fei, *Appl. Catal., B* **2023**, *324*, 122267; c) M. Yan, Z. Wei, Z. Gong, B. Johannessen, G. Ye, G. He, J. Liu, S. Zhao, C. Cui, H. Fei, *Nat. Commun.* **2023**, *14*, 368.

[5] a) M. F. Li, Z. P. Zhao, T. Cheng, A. Fortunelli, C. Y. Chen, R. Yu, Q. H. Zhang, L. Gu, B. V. Merinov, Z. Y. Lin, E. B. Zhu, T. Yu, Q. Y. Jia, J. H. Guo, L. Zhang, W. A. Goddard, Y. Huang, X. F. Duan, *Science* **2016**, *354*, 1414; b) L. Chong, J. G. Wen, J. Kubal, F. G. Sen, J. X. Zou, J. Greeley, M. Chan, H. Barkholtz, W. J. Ding, D. J. Liu, *Science* **2018**, *362*, 1276; c) X. Q. Huang, Z. P. Zhao, L. Cao, Y. Chen, E. B. Zhu, Z. Y. Lin, M. F. Li, A. M. Yan, A. Zettl, Y. M. Wang, X. F. Duan, T. Mueller, Y. Huang, *Science* **2015**, *348*, 1230; d) S. Siahrostami, A. Verdaguer-Casadevall, M. Karamad, D. Deiana, P. Malacrida, B. Wickman,

M. Escudero-Escribano, E. A. Paoli, R. Frydendal, T. W. Hansen, I. Chorkendorff, I. E. L. Stephens, J. Rossmeisl, *Nat. Mater.* **2013**, *12*, 1137; e) J. S. Jirkovský, I. Panas, E. Ahlberg, M. Halasa, S. Romani, D. J. Schiffrin, *J. Am. Chem. Soc.* **2011**, *133*, 19432; f) A. Verdaguer-Casadevall, D. Deiana, M. Karamad, S. Siahrostami, P. Malacrida, T. W. Hansen, J. Rossmeisl, I. Chorkendorff, I. E. L. Stephens, *Nano Lett.* **2014**, *14*, 1603.

[6] a) Y. Gao, B. Liu, D. Wang, *Adv. Mater.* **2023**, *35*, 2209654; b) J. S. Bates, M. R. Johnson, F. Khamespanah, T. W. Root, S. S. Stahl, *Chem. Rev.* **2022**, *123*, 6233; c) X. Guo, J. Zhang, L. Yuan, B. Xi, F. Gao, X. Zheng, R. Pan, L. Guo, X. An, T. Fan, S. Xiong, *Adv. Energy Mater.* **2023**, *13*, 2204376.

[7] a) S. Chen, T. Luo, X. Li, K. Chen, J. Fu, K. Liu, C. Cai, Q. Wang, H. Li, Y. Chen, C. Ma, L. Zhu, Y.-R. Lu, T.-S. Chan, M. Zhu, E. Cortés, M. Liu, *J. Am. Chem. Soc.* **2022**, *144*, 14505; b) Y. Jia, Z. Xue, J. Yang, Q. Liu, J. Xian, Y. Zhong, Y. Sun, X. Zhang, Q. Liu, D. Yao, G. Li, *Angew. Chem. Int. Ed.* **2022**, *61*, e202110838; c) E. Jung, H. Shin, B.-H. Lee, V. Efremov, S. Lee, H. S. Lee, J. Kim, W. Hooch Antink, S. Park, K.-S. Lee, S.-P. Cho, J. S. Yoo, Y.-E. Sung, T. Hyeon, *Nat. Mater.* **2020**, *19*, 436.

[8] a) L. Zong, K. Fan, L. Cui, F. Lu, P. Liu, B. Li, S. Feng, L. Wang, *Angew. Chem. Int. Ed.* **2023**, *62*, e202309784; b) W. Song, C. Xiao, J. Ding, Z. Huang, X. Yang, T. Zhang, D. Mitlin, W. Hu, *Adv. Mater.* **2023**, *36*, 2301477.

[9] a) Q. Yang, W. Xu, S. Gong, G. Zheng, Z. Tian, Y. Wen, L. Peng, L. Zhang, Z. Lu, L. Chen, *Nat. Commun.* **2020**, *11*, 5478; b) E. Zhang, L. Tao, J. An, J. Zhang, L. Meng, X. Zheng, Y. Wang, N. Li, S. Du, J. Zhang, D. Wang, Y. Li, *Angew. Chem. Int. Ed.* **2022**, *61*, e202117347; c) X. Guo, J. Shi, M. Li, J. Zhang, X. Zheng, Y. Liu, B. Xi, X. An, Z. Duan, Q. Fan, F. Gao, S. Xiong, *Angew. Chem. Int. Ed.* **2023**, *62*, e202314124.

[10] Z. Lin, H. Huang, L. Cheng, W. Hu, P. Xu, Y. Yang, J. Li, F. Gao, K. Yang, S. Liu, P. Jiang, W. Yan, S. Chen, C. Wang, H. Tong, M. Huang, W. Zheng, H. Wang, Q. Chen, *Adv. Mater.* **2021**, *33*, 2107103.

[11] M. Jia, S. Hong, T.-S. Wu, X. Li, Y.-L. Soo, Z. Sun, *Chem. Commun.* **2019**, *55*, 12024.

[12] H. Zhang, F. Wan, X. Li, X. Chen, S. Xiong, B. Xi, *Adv. Funct. Mater.* **2023**, *33*, 2306340.

[13] a) Z. Yang, Z. Yao, G. Li, G. Fang, H. Nie, Z. Liu, X. Zhou, X. a. Chen, S. Huang, *ACS Nano* **2012**, *6*, 205; b) Y. Mun, S. Lee, K. Kim, S. Kim, S. Lee, J. W. Han, J. Lee, *J. Am. Chem. Soc.* **2019**, *141*, 6254.

[14] H. Liu, Y. Liu, D. Zhu, *J. Mater. Chem.* **2011**, *21*, 3335.

[15] a) Z. Teng, Q. Zhang, H. Yang, K. Kato, W. Yang, Y.-R. Lu, S. Liu, C. Wang, A. Yamakata, C. Su, B. Liu, T. Ohno, *Nat. Catal.* **2021**, *4*, 374; b) Z. Jiang, T. Wang, J. Pei, H. Shang, D. Zhou, H. Li, J. Dong, Y. Wang, R. Cao, Z. Zhuang, W. Chen, D. Wang, J. Zhang, Y. Li, *Energy Environ. Sci.* **2020**, *13*, 2856.

[16] H. Gong, Z. Wei, Z. Gong, J. Liu, G. Ye, M. Yan, J. Dong, C. Allen, J. Liu, K. Huang, R. Liu, G. He, S. Zhao, H. Fei, *Adv. Funct. Mater.* **2022**, *32*, 2106886.

[17] J. P. Perdew, K. Burke, M. Ernzerhof, *Phys. Rev. Lett.* **1996**, *77*, 3865.

[18] S. Grimme, S. Ehrlich, L. Goerigk, *J. Comput. Chem.* **2011**, *32*, 1456.

[19] D. A. McQuarrie, *Statistical Mechanics*, University Science Books, **2000**.

[20] V. Wang, N. Xu, J.-C. Liu, G. Tang, W.-T. Geng, *Comput. Phys. Commun.* **2021**, *267*, 108033.